Journal of MATERIALS RESEARCH

Article
DOI: 10.1557/jmr.2019.18

NANOCRYSTALLINE HIGH ENTROPY MATERIALS: PROCESSING CHALLENGES AND PROPERTIES

FOCUS ISSUE

Materials-structure-property correlation study of spark plasma sintered AlCuCrFeMnW$_x$ (x = 0, 0.05, 0.1, 0.5) high-entropy alloys

Devesh Kumar[1,2], Vishnu K. Sharma[1], Y.V.S.S. Prasad[1], Vinod Kumar[3,a]

[1]Department of Metallurgical and Materials Engineering, Malaviya National Institute of Technology (MNIT) Jaipur, 302017, India
[2]Department of Mechanical Engineering Jaipur Engineering College and Research Centre (JECRC), Jaipur 302017, India
[3]Discipline of Metallurgy and Materials Science, Indian Institute of Technology (IIT) Indore, 453552, India
[a]Address all correspondence to this author. e-mail: vk.iitk@gmail.com

Received: 4 July 2018; accepted: 2 January 2019

A novel series of nanocrystalline AlCuCrFeMnW$_x$ (x = 0, 0.05, 0.1, 0.5) high-entropy alloys (HEAs) were synthesized by mechanical alloying followed by spark plasma sintering. The phase evolution of the current HEAs was studied using X-ray diffraction (XRD), transmission electron microscopy, and selected area electron diffraction. The XRD of the AlCuCrFeMn sintered HEA shows evolution of ordered B2 phase (AlFe type), sigma phase (Cr rich), and FeMn phase. AlCuCrFeMnW$_x$ (x = 0.05, 0.1, 0.5 mol) shows formation of ordered B2 phases, sigma phases, FeMn phases, and BCC phases. Micro-hardness of the AlCuCrFeMnW$_x$ samples was measured by Vickers microindentation and the maximum value observed is 780 ± 12 HV. As the tungsten content increases, the fracture strength under compression increases from 1010 to 1510 MPa. Thermodynamic parameters of present alloys confirm the crystalline phase formation, and finally structure–property relationship was proposed by conventional strengthening mechanisms.

Introduction

High-entropy alloys (HEAs) are a comparatively new breed of materials of general interest in the metallurgical research community in recent years. They are classified by their unconventional composition, as they do not surround a single main component, but instead contain more than one elements [1, 2]. Based on the indication already existing in the literature to date, it seems to be that the core effects of HEAs related with entropy stabilization, lattice distortion, and sluggish diffusion may not be as prominent as initially proposed. Few examples of HEAs are considered to be entropy-stable solid solutions: both experiments and theories show that adding more components to the alloy can lead to intermetallic formation or phase separation. There are some recent thoughts about alternative naming conventions, like "compositionally complex alloys" or "complex concentrated alloys'". Still, the author argues that since the terminology of "HEA" is so ingrained in the discourse, changes in the naming convention can only lead to confusion [3, 4, 5]. In general, good corrosion resistance, toughness, and oxidation resistance will be required alongside strength. HEA research often adds elements directly to the resulting mechanical properties [6, 7, 8]. Similarly, several HEAs are composed with refractory metal elements, and they show high strength and low ductility [9, 10]. Tungsten has good performance at high temperatures with a high melting point, and there are not many literature works found in the field of HEA. Recently, CrFeNiV$_{0.5}$W$_x$ and CrFeNi$_2$V$_{0.5}$W$_x$ high-entropy alloys were synthesized by arc melting [11].

Several HEA alloy systems have been formed by arc melting and casting paths [12, 13], but the main disadvantage of this route is the development of dendrites and the selective segregation of binding elements during solidification. Further heat treatment steps are generally required to homogenize the cast structure. Two common methods for strengthening of materials are grain refinement and solid solution strengthening [14]. Furthermore to structural improvements, mechanical alloying is used to confirm uniform mixing of the contributing elements. In the spark plasma sintered (SPSed) AlCuCrFeMnW$_x$ (x = 0, 0.05, 0.1, 0.5 mol) alloy system, phase transformations and alloying behavior were studied by

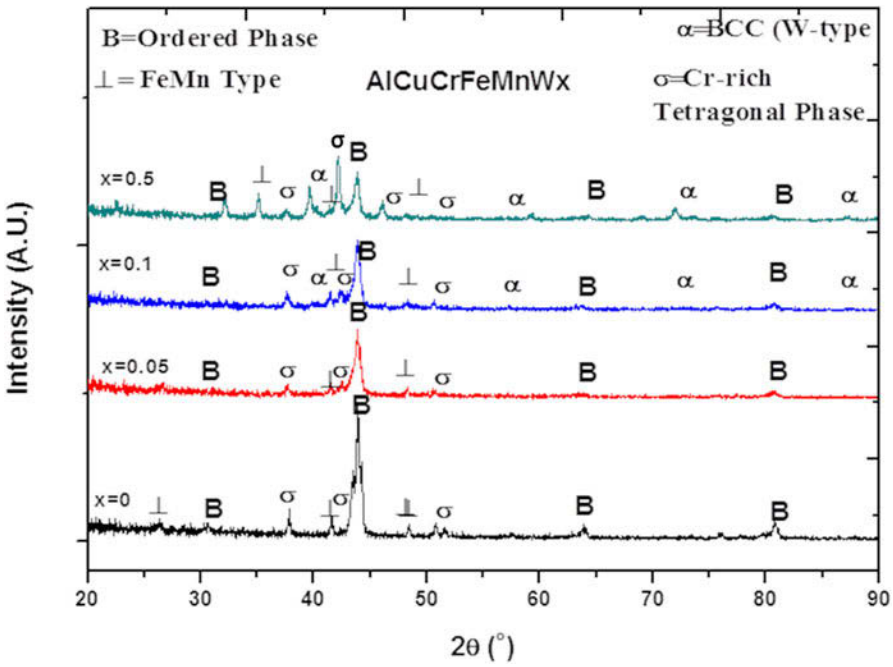

Figure 1: XRD patterns of $AlCuCrFeMnW_x$ (x = 0, 0.05, 0.1, 0.5 mol) HEAs after SPS.

variable W content. Mechanical properties were evaluated using Vickers hardness tester and Instron testing machine. A well thinking of the phase prediction mechanism and the strengthening mechanisms of $AlCuCrFeMnW_x$ HEAs are very important and interesting. Finally, the results are interrelated to the thermodynamic parameters, and based on the theory of conventional strengthening, the structure–property relationship is proposed.

Results

Crystal structure and microstructures

The experimental density of consolidated alloys was measured by Archimedes theory, and the relative density was measured by ImageJ analysis. It is seen that the relative density of 94–96% for each alloy system confirms the lower porosity in the sintered alloy.

Phase analysis (Fig. 1) by X-Ray diffraction (XRD) suggests that as-milled $AlCuCrFeMnW_x$ (x = 0, 0.05, 0.1, 0.5 mol) HEAs have been consolidated by spark plasma sintering at 900 °C. The microstructure of sintered $AlCuCrFeMnW_x$ (x = 0.05, 0.1, 0.5 mol) HEAs contained of major AlFe type ordered phase (JCPDS: 00-033-0020), BCC phase, and FeMn phase (JCPDS: 01-071-8284) with some minor peaks of σ phase Cr-rich tetragonal phase (JCPDS: 01-071-7530), and the microstructure of AlCuCrFeMn is AlFe type ordered structure phase, FeMn phase, and Cr-rich σ phase precipitates. The development and progress of Cr-rich precipitates in FeMn phase in $AlCuCrFeMnW_x$ HEAs are due to high positive enthalpy between the binary elements, such as Cu–Cr and Cr–Mn [21].

Table I shows results of XRD analysis with lattice parameter, phase fraction, crystallite size, and lattice strain of the bulk $AlCuCrFeMnW_x$ (x = 0, 0.05, 0.1, 0.5 mol) HEAs. Instrumental broadening was corrected using single crystal Si wafer. Lattice strain (ε) was calculated by Eq. (1), where β_{hkl} is the full-width half maximum (FWHM) [4].

$$\varepsilon = \beta_{hkl}/4\tan\theta \quad . \tag{1}$$

Figures 2(a)–2(d) illustrate the back-scattered electron (BSE) images of $AlCuCrFeMnW_x$ (x = 0, 0.05, 0.1, 0.5 mol) HEAs. Although the atomic numbers of the alloying elements are very close, the BSE contrast exposes the existence of four phases. According to EDS composition analysis (Supplementary material), coarse type AlFe phase observed correspond to ordered phase B2, phase FeMn seems to be spread along the ordered phase network, Cr-rich tetragonal closed packed (TCP) phase, and BCC phase are observed.

Figure 3(a) displays bright-field images of AlCuCrFeMn sintered at 900 °C and related SAED patterns which are categorized by tetragonal phase precipitates, FeMn phase, and ordered B2 phase [SAED, Figs. 3(b) and 3(c)]. Figure 4(a) illustrates bright-field microstructure of $AlCuCrFeMnW_{0.05}$, and related SAED patterns are characterized by tetragonal phase precipitates, an FeMn type phase, BCC phase, and ordered B2 phase [SAED, Figs. 4(b) and 4(c)]. Figures 5(a) and 6(a) show BSE micrograph of $AlCuCrFeMnW_{0.1}$ and

TABLE I: Phase fraction, lattice parameter, crystalline size, lattice strain, and electronegativity difference (ΔX) of AlCuCrFeMnW$_x$ HEAs.

Composition	Phases	Phase fraction	Lattice parameter (pm)	Crystallite size (nm)	Lattice strain (%)	Electronegativity difference (ΔX)
AlCuCrFeMnW$_{0.5}$	Ordered	0.315	317.12	50.12	0.32	0.269
	FeMn type	0.089	a = 879.62, c = 456.82	34.98	0.31	
	BCC	0.292	289.12	63.78	0.27	
	Sigma	0.314	370.88	78.98	0.30	
AlCuCrFeMnW$_{0.1}$	Ordered	0.501	317.92	58.12	0.30	0.266
	FeMn type	0.121	a = 878.62, c = 456.98	64.98	0.29	
	BCC	0.212	287.12	93.78	0.25	
	Sigma	0.298	368.88	68.98	0.31	
AlCuCrFeMnW$_{0.05}$	Ordered	0.687	317.92	78.12	0.30	0.260
	FeMn type	0.134	a = 878.62, c = 456.98	94.98	0.29	
	BCC	0.089	287.12	123.98	0.25	
	Sigma	0.283	36	88.88	0.31	
AlCuCrFeMn	Ordered	0.765	a = 868.62, c = 466.98	104.98	0.27	0.252
	FeMn type	0.105	289.12	133.98	0.23	
	Sigma	0.153	369.88	98.88	0.30	

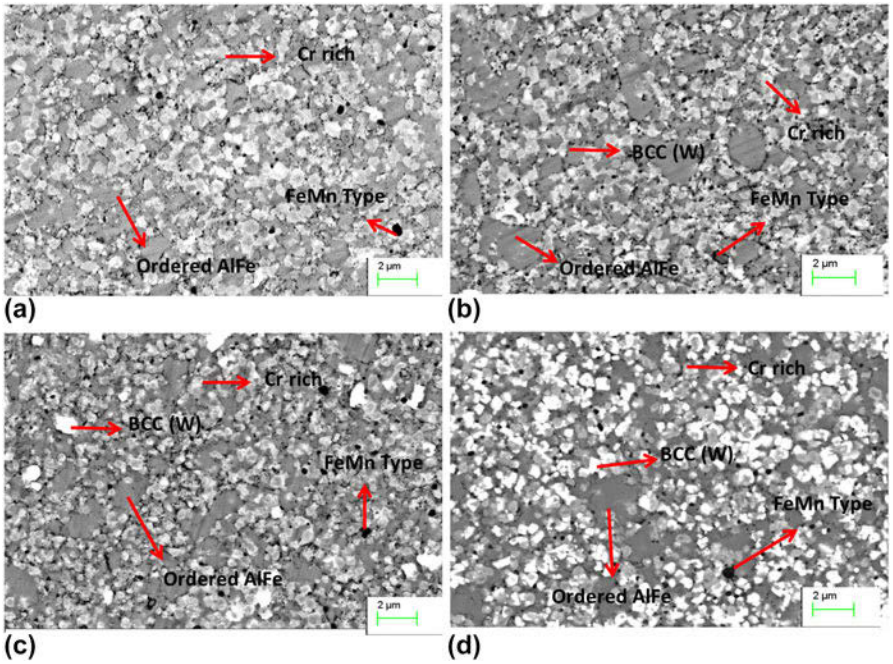

Figure 2: SEM back-scattered images of AlCuCrFeMnW$_x$ (x = 0, 0.05, 0.1, 0.5 mol) HEAs.

AlCuCrFeMnW$_{0.5}$ sintered at 900 °C. SAED patterns are tetragonal phase precipitates, an FeMn type phase, and ordered B2 phase for both HEAs [SAED, Figs. 5(b) and 5(c) and Figs. 6(b) and 6(c)]. The average crystallite size is 30–100 nm, which is equivalent to that achieved by the Scherrer formula (Table I). Calculating the distinct crystallite sizes of all four phases from the dark-field image [Figs. 3–6(d)] were not possible due to the closeness of the diffraction rings of these phases.

Mechanical properties of AlCuCrFeMnW$_x$ HEAs

Microhardness value was determined using Vickers microhardness tester on AlCuCrFeMnW$_x$ HEAs, and Vickers microhardness test was repeated five times across the polished sample surface. The hardness values of AlCuCrFeMnW$_x$ (x = 0, 0.05, 0.1, 0.5 mol) were determined to be 633.5 ± 11.5 HV to 780 ± 12 HV as the tungsten content increases [Fig. 7(a)].

The hardness shown is nearly linearly increased with increased tungsten content, and it can be expressed as follows:

$$Y(\mathrm{HV}) = 281.91X + 629.67 \quad , \qquad (2)$$

where Y is the microhardness value in HV and X is the W content in mol.

An experiential relationship between the yield strength (Y) and hardness value is given by (Table II): [16].

$$\sigma_{\mathrm{Y}}(\mathrm{MPa}) = 3XH_{\mathrm{V}}(\mathrm{HVN}) \quad . \qquad (3)$$

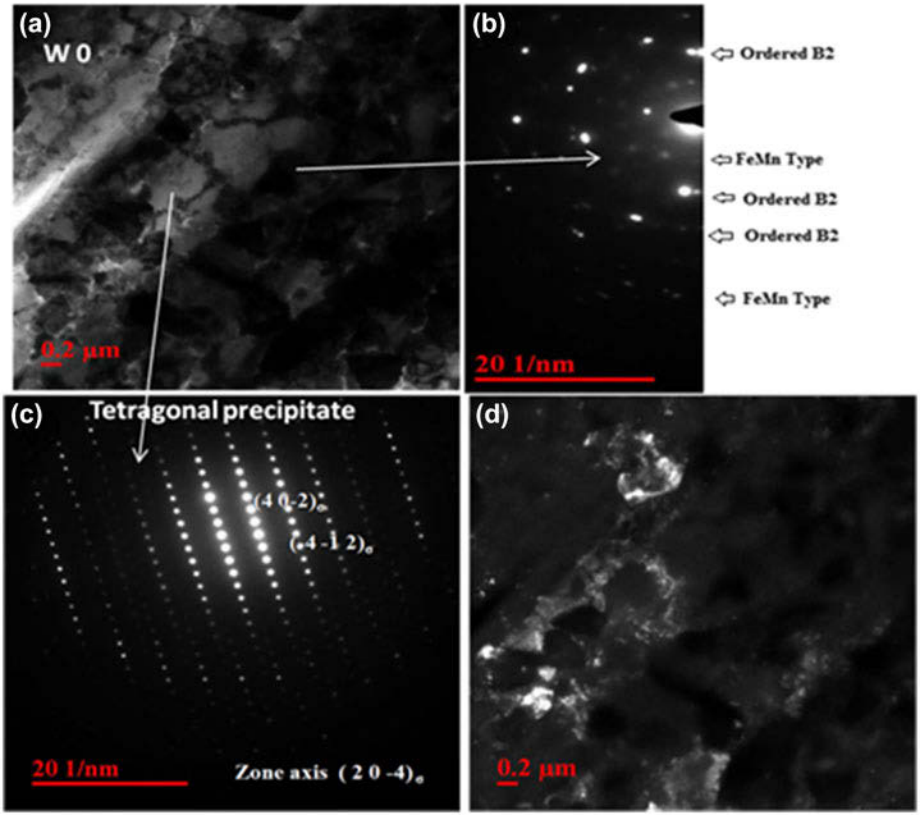

Figure 3: (a) TEM bright-field image showing different morphologies; (b) SAED pattern of FeMn and B2 type phases in TEM image; (c) SAED pattern tetragonal phase in TEM image; and (d) TEM dark-field image of AlCuCrFeMn HEA.

Engineering stress–strain curves under compression mode for the present HEAs having different amounts of the refractory element (W) are shown in Fig. 7(b), and the results of fracture strength under compression are shown in Table II. It is noticed that fracture strength of present alloy system has a noticeable effect with increasing tungsten content. The tungsten-free alloy (W_0) has a low yield strength of 1010 MPa. The $W_{0.05}$ alloy shows very similar behavior; however, its fracture strength under compression value (1120 MPa) is greater than the W_0 alloy. Fracture strength under compression of the $W_{0.1}$ alloy is 1250 MPa but increases rapidly to 1510 MPa for $W_{0.5}$ alloy. The development of the disordered BCC phases and tetragonal phases expressively improves the hardness and strength of the present HEAs. Generally, energy absorbed before fracture in compression is called toughness. So according to Fig. 7(b), toughness of present HEAs increases with the increase in tungsten content.

Discussion

Thermodynamic parameters

The morphology and phases of AlCuCrFeMnW_x HEAs can be described by thermodynamics parameters. Enthalpy of mixing of binary elements played an important role in formation of solid solution such as Fe–Mn (−2.9 kJ/mol) and Al–Fe (−11 kJ/mol) [17], which is thermodynamically more favorable [mixing enthalpy of each binary element is shown in Supplementary material]. Thus, larger portion of the microstructure consists of Fe–Mn and Al–Fe ordered phase (Fig. 2) in low tungsten containing AlCuCrFeMnW_x (x = 0, 0.05, 0.1) HEAs and major fraction of BCC phase (W type) in AlCuCrFeMn$W_{0.5}$ HEA. In addition, AlCuCrFeMnW_x HEAs partially fulfill the Zhang's [18] criterion for the development of simple solid solution; -10 kJ/mol $< \Delta H_{\mathrm{mix}} < 5$ kJ/mol and $\delta < 4\%$. Thus, solid solution and intermetallics in AlCuCrFeMnW_x HEAs are formed due to larger atomic size difference (δ) [21].

Electronegativity is a tendency of an atom to attract an electron and as per the Hume-Rothery rules, large electronegativity of a solute can lead to the formation of intermetallic compounds. In, HEAs, the electronegativity difference (ΔX) is given by Eq. (4) [19, 20].

$$\Delta X = \sqrt{\sum_{i=1}^{N} c_i \left(X_i - X_{\mathrm{avg}}\right)^2} \quad , \tag{4}$$

where X_i is the Pauling electronegativity for the ith element and $X_{\mathrm{avg}} = \sum_{i=1}^{N} c_i X_i$.

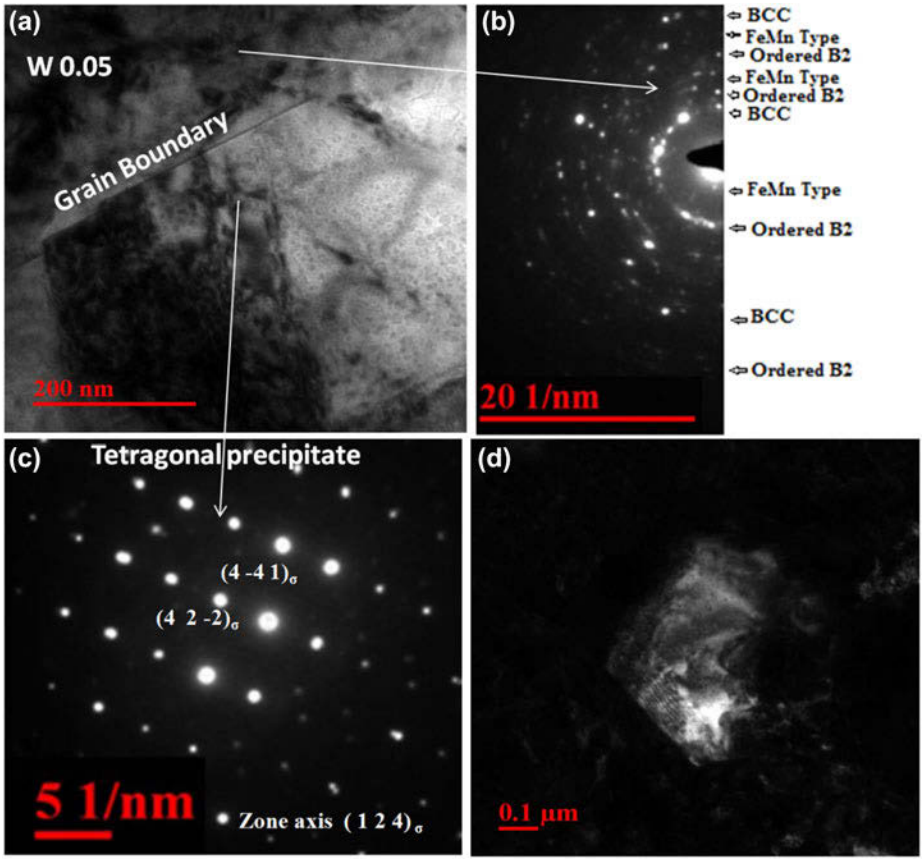

Figure 4: (a) TEM bright-field image showing different morphologies; (b) SAED pattern of FeMn type, BCC, and B2 type phases in TEM image; (c) SAED pattern tetragonal phase in TEM image; and (d) TEM dark-field image of $AlCuCrFeMnW_{0.05}$ HEA.

The effect of electronegativity on the stability of phases was given by Dong et al. [20]. According to Dong et al. when $\Delta X > 0.133$, HEAs forms stable TCP structure. $AlCuCrFeMnW_x$ alloys having a range of ΔX are 0.252–0.269.

It is believed that ΔH_{mix} and δ are important parameters for the stability of solid solution, which has been reflected in most of the criteria used. Valence electron concentration (VEC) seems to correlate well with the crystalline structure of HEA, the FCC structure consistently associated with high VEC value, and the BCC structure associated with low VEC value [21]. Tsai et al. [22] have used VEC alongside compositional considerations to predict Cr-rich tetragonal sigma phase (σ) formation in HEAs, while others have compared instances of ordered phase formation (including tetragonal close-packed phases, TCPs) against the average value of the *d*-orbital energy level and electronegativity difference (ΔX). Table I shows phase fraction, lattice parameter, crystalline size, lattice strain, and electronegativity difference (ΔX) of $AlCuCrFeMnW_x$ HEAs.

Strengthening mechanism

The $AlCuCrFeMnW_x$ powder contains a relatively minor fraction of FCC phase as compared to BCC phase matrix [21]. After sintering, BCC and FCC phases are completely transformed into AlFe type ordered structure, FeMn phase, and Cr-rich sigma (σ) phase. Interestingly, the $AlCuCrFeMnW_x$ alloys form nanocrystalline bulk products due to the high heating rate of 100 °C/min essential in SPS processes. The high heating rate does prevent grain coarsening, while achieving high densification.

The excellent fracture strength under compression of these HEAs is due to the second-stage hardening (tetragonal phase) and solution strengthening (W rich). As presented in Fig. 7(b), the alloys W_0 and $W_{0.05}$ show good plasticity due to existing of ordered phases, but in $W_{0.1}$ and $W_{0.5}$ alloys, its shows excellent fracture strength because of increase in brittle phases. For an HEA, each atom is considered as solute atom that occupies random points of the lattice. The atomic size difference and other properties of these solute atoms lead to severe distortion of the lattice. The interaction between different atoms leads to the development of a local elastic stress that prevents the movement of dislocations, with a consequent increase in strength.

In the $AlCuCrFeMnW_x$ alloys, the increase in hardness with increasing tungsten content is shown in Fig. 7(a). The

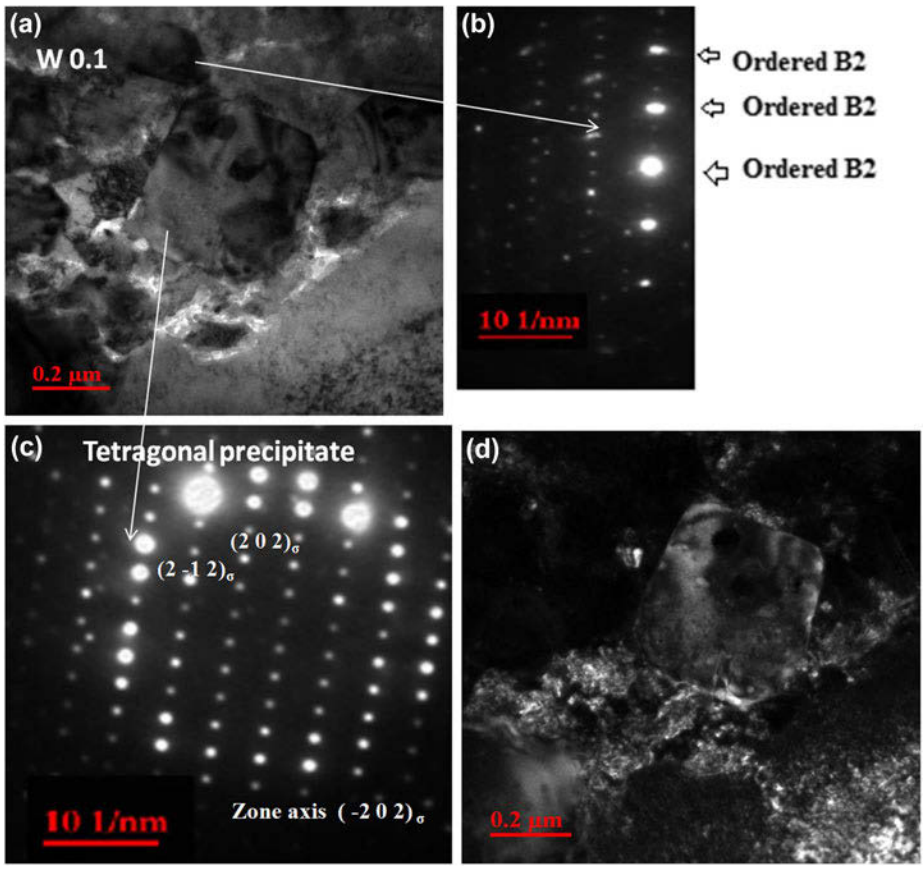

Figure 5: (a) TEM bright-field image showing different morphologies; (b) SAED pattern of FeMn type and B2 type phases in TEM image; (c) SAED pattern tetragonal phase in TEM image; and (d) TEM dark-field image of $AlCuCrFeMnW_{0.1}$ HEA.

microhardness value of $AlCuCrFeMnW_{0.5}$ alloy shows a maximum hardness of 780 ± 12 HV, and then the hardness value decreases with decreasing tungsten content and lowest hardness in the case of AlCuCrFeMn HEA is 633 ± 11.50 HV. The high hardness value of these HEAs is due to the collective effect of grain size, solid solution, and strengthening by precipitation. Using the Tabor's equation [23], $H = 3\sigma_{flow}$, where H is the hardness and σ_{flow} is the slip/yield flow of the material. For AlCuCrFeMn, $AlCuCrFeMnW_{0.05}$, $AlCuCrFeMnW_{0.1}$, and $AlCuCrFeMnW_{0.5}$ (Table II), σ_{flow} is calculated as 2059, 2223, 2304, and 2549 MPa, respectively. Furthermore, this is a four-phase structure composed of two solid solutions (BCC and B2). Thus, the complete flow stress is determined by combination of lattice stress friction mobile dislocations, strengthening due to intersecting dislocations (Taylor reinforcement), grain refinement (Hall–Petch strengthening), and solid solution strengthening. It is proposed that the following equations are used to decide the different mechanism contributing to the flow stress [24]:

$$\Delta_{flow} = \sigma_i + \Delta\sigma_{SH} + \Delta\sigma_{HP} + \Delta\sigma_{SS} \quad , \tag{5}$$

where σ_i is the frictional stress and it is present in the lattice of all elements. Because these HEAs have recently issued new classes of alloys, as per the authors' knowledge, their friction stress data are not available in the literature. Frictional stresses calculated by the rule of mixture is shown in Table III [22].

$\Delta\sigma_{SH}$ (strain hardening) is the relatively large grains strengthening due to the intersection of dislocations during deformation [24].

$$\Delta\sigma_{SH} = M\alpha Gb\rho^{1/2} \quad , \tag{6}$$

where M is the Taylor factor (both FCC and BCC materials are 3.06) and α is the material-specific correction factor. It is assumed that α is unity because of novelty of HEAs. G is the shear module, b is the Burgers vector, and ρ is the dislocation density. Shear modulus (G) is determined by $G = E/2\ (1 + \nu)$, where ν is the Poisson's ratio (0.33). The Burgers vector for a BCC-based lattice is calculated as $b = (a/2)\ (111)$. Dislocation density (ρ) is calculated by the following equation [25]:

$$\rho = \frac{2\sqrt{3}\varepsilon}{db} \quad . \tag{7}$$

In this Eq. (7), ε is lattice strain, d is grain size (nm), and b is the Burgers vector (nm). $\Delta\sigma_{SH}$ strain hardening of this material is shown in Table III using Eq. (6).

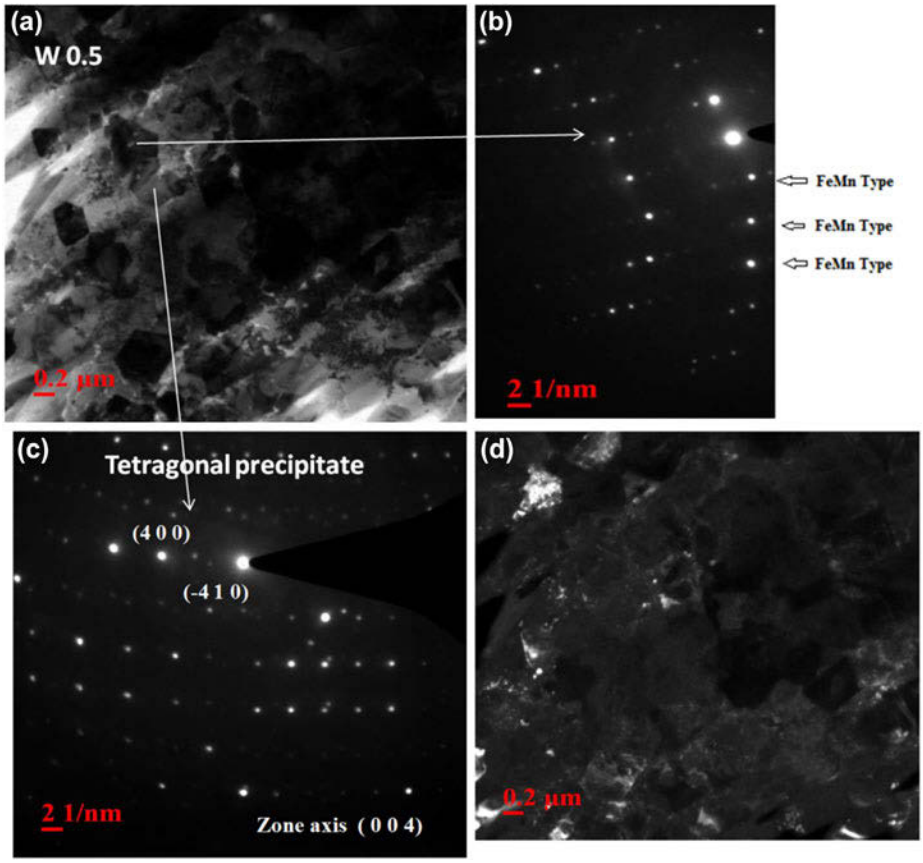

Figure 6: (a) TEM bright-field image showing different morphologies; (b) SAED pattern of FeMn type phase in TEM image; (c) SAED pattern tetragonal phase in TEM image; and (d) TEM dark-field image of $AlCuCrFeMnW_{0.5}$ HEA.

TABLE II: Microhardness (HV), microhardness (MPa), yield strength (MPa) and elastic modulus (MPa) of $AlCuCrFeMnW_x$ (x = 0, 0.05, 0.1, 0.5 mol) HEAs.

Composition	Micro-hardness (HV)	Micro-hardness (MPa)	Tensile yield strength (MPa)	Compressive strength (MPa)
AlCuCrFeMn	633	6178	2059	1010
$AlCuCrFeMnW_{0.05}$	680	6669	2223	1120
$AlCuCrFeMnW_{0.1}$	705	6914	2304	1250
$AlCuCrFeMnW_{0.5}$	780	7649	2549	1510

$\Delta\sigma_{HP}$ is the Hall–Petch strengthening and is calculated by [24]:

$$\Delta\sigma_{HP} = K_{HP} d^{-0.5} \quad , \tag{8}$$

where K_{HP} is the Hall–Petch constant and 'd' is the average particle size, and Table III estimates the Hall–Petch strengthening involvement.

$\Delta\sigma_{SS}$ is the contribution of the solid strengthening of the solution. In the conventional binary solid solution, the elastic interaction between the dislocations and the stress field caused by the solute atoms determines the appropriate strengthening mechanism, and all models of strengthening mechanism of the solid solution are effective for the binary solid solution [26, 27]. Because HEA is a complex concentrated alloy, Senkov et al. [28] proposed the following formula to estimate the strengthening of the solid solution of a concentrated system:

$$\Delta\sigma_{SS} = AG\varepsilon^{4/3}C^{2/3} \quad . \tag{9}$$

In Eq. (9), A is a dimensionless number of about 0.1. C is the atomic concentration of the solute (0.16), G is the shear module of the alloy, and ε is the strain of the lattice caused by the solute. Based on the calculation and formula used in Eq. (5), the total contribution of various reasonable mechanisms to the flow σ_{flow} is from 2039 to 2460 MPa to increase the content of tungsten. The Vickers hardness (HV) of these HEAs was observed for increasing the tungsten content from 6178 to 7469 MPa (Table II). Thus, the ratio of these alloys (H/σ_{flow}) is 3.02–3.04. As per Tabor's analysis [23], the ratio between these traditional materials varies from 2.8 to 3.2. Therefore, the calculated ratio of 3 in case of present HEAs is in close agreement with that of conventional polycrystalline materials. From Table III, it is clear that the Taylor hardening

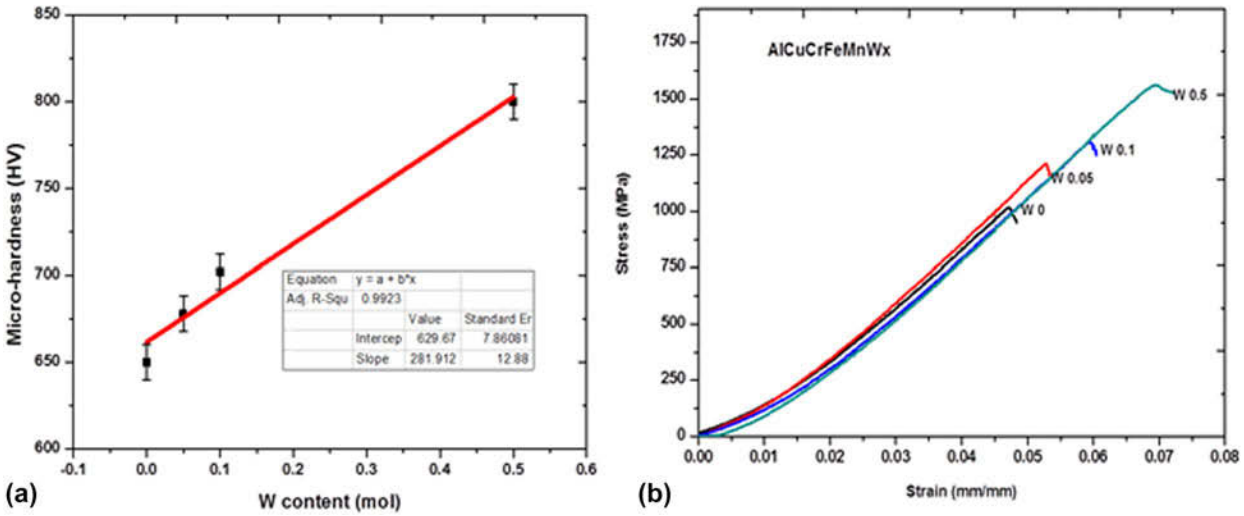

Figure 7: Microhardness and stress–strain curve under compression mode of AlCuCrFeMnW$_x$ (x = 0, 0.05, 0.1, 0.5 mol) HEAs.

TABLE III: Frictional stress (σ_i), strain hardening ($\Delta\sigma_{SH}$), grain size strengthening ($\Delta\sigma_{HP}$), solid solution strengthening ($\Delta\sigma_{SS}$), and yield Strength of AlCuCrFeMnW$_x$ (x = 0, 0.05, 0.1, 0.5 mol) HEAs.

	Frictional stress (σ_i) MPa	Strain hardening ($\Delta\sigma_{SH}$) MPa	Grain size strengthening ($\Delta\sigma_{HP}$) MPa	Solid solution strengthening ($\Delta\sigma_{SS}$) MPa	Tensile yield strength total (MPa)
AlCuCrFeMn	180	1090	502	267	2039
AlCuCrFeMnW$_{0.05}$	195	1170	591	284	2240
AlCuCrFeMnW$_{0.1}$	198	1201	609	290	2298
AlCuCrFeMnW$_{0.5}$	209	1291	659	301	2460

and the strengthening of the grain size are the main strengthening mechanisms of these alloys, which represent almost 80% of the stress of the flow.

For HEAs, the terms "solute" and "solvent" lose their conventional meanings; thus, the precise contribution of solid solution strengthening in HEAs remains to be a challenge. Fortunately, Fe, Cr, Mn, and Cu elements have nearly the same atomic sizes, and the mixing enthalpies of different atom pairs of these four elements are nearly equal to zero. When incorporating tungsten elements at a low level to the AlCuCrFeMn matrix, the element will act as the solute atoms, a standard model for substitutional solid solution strengthening based on dislocation-solute elastic interactions could be directly applied to evaluate the potency of solution strengthening (BCC Phase) caused by the solute atom of tungsten. Clearly, the experimental data are much higher than those of the theoretical value, suggesting an extra hardening besides the solid solution strengthening. There are other apparent reasons, such as the segregation of tungsten and particle precipitation in the SPSed W$_{0.1}$ and W$_{0.5}$ alloys which are more effective on strengthening than just solid solution hardening.

It can be seen that AlCuCrFeMnW$_x$ alloys have better hardness and high fracture strength under compression; therefore, it can be considered potential candidates for structural application.

Conclusion

As-milled AlCuCrFeMnW$_x$ HEAs are successfully consolidated by spark plasma sintering at 900 C and 50 MPa. The XRD results of the AlCuCrFeMn alloy show that the ordered B2 phase, sigma phase (Cr-rich), FeMn phase, and AlCuCrFeMnW$_x$ (x = 0.05, 0.1 0.5 mol) show the formation of ordered B2 phases (AlFe type), sigma phases (Cr-rich), FeMn phases, and BCC phases. The relative density of these HEAs reaches 94–96% of the theoretical density, with an excellent Vickers hardness up to 780 HV. As the W content increases, the fracture strength under compression increases from 1010 to 1510 MPa. The volumetric fraction of the BCC structure phase increases with the increase in the tungsten content, and the presence of tetragonal phases is the main reason for the increase in Vickers hardness and compressive strength.

Experimental procedures

Sample preparation

Elemental high-purity powders of Al, Fe, Cu, Cr, Mn, and W of purity greater than 99.9% and mesh size of 200–300 were

mechanically alloyed using Pulverisette-P7 high-energy planetary ball mill (Fritsch, Germany) using a vial and balls of tungsten carbide. Ball to powder weight ratio was maintained to be around 10:1. Toluene is used as a process controlling agent (PCA) to prevent excessive cold welding on the surface of the ball and vial and also to provide the reducing media during milling. Milling was carried out up to 20 h in a planetary ball mill at 300 rpm. As-milled powders of $AlCuCrFeMnW_x$ ($x = 0$, 0.05, 0.1, 0.5 mol) alloys are spark plasma sintered using Dr. Sinter (Model- S625) at 900 °C. For present alloys, the holding time, heating rate, and applied pressure were 10 min, 100 °C/min, and 50 MPa, respectively. Generally, sintering temperature is defined as to be around 0.5–0.7T_m, where T_m is the melting temperature. The density of bulk sample is measured using density measurement machine (Mettler Toledo) in an ethanol medium [15].

Characterization and mechanical properties

Phase changes of current HEAs were characterized by X-ray diffractometer (XRD) using X'pert Pro (Malvern Panalytical Malvern, United Kingdom) with a Cu K_α ($\lambda = 0.1540598$ nm) source. Single crystal Si wafer was used for correction in instrumental broadening. Microstructure of the bulk sample was studied by FE-SEM (Nova Nano 450, FEI Eindhoven, The Netherlands) and elemental composition by an EDS detector (Bruker Coventry, United Kingdom). Phase formation was analyzed using TEM (Tecnai 20, FEI Eindhoven, The Netherlands), which was operated at 200 kV. The microhardness of consolidated samples was determined using a Vickers microhardness tester at a load of 200 gf and a dwell time of 15 s. Compressive properties were tested using an Instron UTM 5500 machine (High Wycombe, United Kingdom) at a loading rate of 0.5 mm/min. The samples were cylindrical, Ø 3 mm × 5 mm, and three tests were done to attain the average value of compressive strength.

Acknowledgment

The authors are thankful to BRNS Project No. 34/20/01/2014-BRNS-0339, Mumbai (India), for financial assistance.

Supplementary material

To view supplementary material for this article, please visit https://doi.org/10.1557/jmr.2019.18.

References

1. **B.S. Murty, J.W. Yeh, and S. Ranganathan**: *High-Entropy Alloy*, 1st ed. (Elsevier Inc., London, 2014).
2. **J.W. Yeh**: Recent progress in high-entropy alloys. *Ann. Chimie Sci. Matériaux* **31**, 633–648 (2006).
3. **J.W. Yeh, S.K. Chen, J.Y. Gan, S.J. Lin, T.S. Chin, T.T. Shun, C.H. Tsau, and S.Y. Chang**: Formation of simple crystal structures in Cu–Co–Ni–Cr–Al–Fe–Ti–V alloys with multiprincipal metallic elements. *Metall. Mater. Trans. A* **35**, 2533–2536 (2004).
4. **O. Maulik, D. Kumar, S. Kumar, D.M. Fabijanic, and V. Kumar**: Structural evolution of spark plasma sintered $AlFeCuCrMg_x$ ($x = 0$, 0.5, 1, 1.7) high entropy alloys. *Intermetallics* **77**, 46–56 (2016).
5. **M.A. Hemphill, T. Yuan, G.Y. Wang, J.W. Yeh, C.W. Tsai, A. Chuang, and P.K. Liaw**: Fatigue behavior of $Al_{0.5}CoCrCuFeNi$ high entropy alloys. *Acta Mater.* **60**, 5723–5734 (2012).
6. **H.W. Yao, J.W. Qiao, M.C. Gao, J.A. Hawk, S.G. Ma, H.F. Zhou, and Y. Zhang**: NbTaV–(Ti, W) refractory high-entropy alloys: Experiments and modeling. *Mater. Sci. Eng., A* **674**, 203–211 (2016).
7. **D.B. Miracle**: Critical assessment 14: High entropy alloys and their development as structural materials. *Mater. Sci. Technol.* **31**, 1142–1147 (2015).
8. **E.J. Pickering and N.G. Jones**: High-entropy alloys: A critical assessment of their founding principles and future prospects. *Int. Mater. Rev.* **61**, 183–202 (2016).
9. **Z.D. Han, H.W. Luan, X. Liua, N. Chen, X.Y. Li, Y. Shao, and K.F. Yao**: Microstructures and mechanical properties of $Ti_xNbMoTaW$ refractory high entropy alloys. *Mater. Sci. Eng., A* **712**, 380–385 (2018).
10. **H.W. Yao, J.W. Qiao, J.A. Hawk, H.F. Zhou, M.W. Chen, and M.C. Gao**: Mechanical properties of refractory high-entropy alloys: Experiments and modeling. *J. Alloys Compd.* **696**, 1139–1150 (2017).
11. **H. Jiang, L. Jiang, K. Han, Y. Lu, T. Wang, Z. Cao, and T. Li**: Effects of tungsten on microstructure and mechanical properties of $CrFeNiV_{0.5}W_x$ and $CrFeNi_2V_{0.5}W_x$ high-entropy alloys. *J. Mater. Eng. Perform.* **24**, 4594–4600 (2015).
12. **X. Xian, L. Lin, Z. Zhong, C. Zhang, C. Chen, K. Song, J. Cheng, and Y. Wu**: Precipitation and its strengthening of Cu-rich phase in $CrMnFeCoNiCu_x$ high-entropy alloys. *Mater. Sci. Eng., A* **713**, 134–140 (2018).
13. **L.J. Zhang, P.F. Yu, M.D. Zhang, D.J. Liu, Z. Zhou, M.Z. Ma, P.K. Liaw, G. Lia, and R.P. Liu**: Microstructure and mechanical behaviors of $Gd_xCoCrCuFeNi$ high-entropy alloys. *Mater. Sci. Eng., A* **707**, 708–716 (2017).
14. **X. Chen, Y. Sui, J. Qi, Y. He, F. Wei, Q. Meng, and Z. Sun**: Microstructure of $Al_{1.3}CrFeNi$ eutectic high entropy alloy and oxidation behavior at 1000 °C. *J. Mater. Res.* **32**, 2109–2116 (2017).
15. **D. Kumar, O. Maulik, S. Kumar, Y.V.S.S. Prasad, and V. Kumar**: Phase and thermal study of equiatomic AlCuCrFeMnW high entropy alloy processed via spark plasma sintering. *Mater. Chem. Phys.* **210**, 71–77 (2018).

16. **F. Khodabakhshi, M. Haghshenas, H. Eskandari, and B. Koohbor**: Hardness-strength relationships in fine and ultra-fine grained metals processed through constrained groove pressing. *Mater. Sci. Eng., A* **636**, 331–339 (2015).
17. **A. Takeuchi and A. Inoue**: Calculations of mixing enthalpy and mismatch entropy for ternary amorphous alloys. *Mater. Trans. JIM* **41**, 1372–1378 (2000).
18. **Y. Zhang, T.T. Zuo, Z. Tang, M.C. Gao, K.A. Dahmen, P.K. Liaw, and Z.P. Lu**: Microstructure and properties of high-entropy alloy. *Prog. Mater. Sci.* **61**, 1–93 (2014).
19. **S. Guo, C. Ng, J. Lu, and C.T. Liu**: Effect of valence electron concentration on stability of fcc and bcc phase in high entropy alloy. *J. Appl. Phys.* **109**, 103505 (2011).
20. **Y. Dong, Y. Lu, L. Jiang, T. Wang, and T. Li**: Effects of electronegativity on the stability of topologically closed packed phase in high entropy alloy. *Intermetallics* **52**, 105e109 (2014).
21. **D. Kumar, O. Maulik, S. Kumar, Y.V.S.S. Prasad, V.K. Sharma, and V. Kumar**: Impact of tungsten on phase evolution in nanocrystalline AlCuCrFeMnW$_x$ (x = 0, 0.05, 0.1, and 0.5 mol) high entropy alloys. *Mater. Res. Express* **4**, 114004 (2018).
22. **M.H. Tsai, K.Y. Tsai, C.W. Tsai, C. Lee, C.C. Juan, and J.W. Yeh**: Criterion for sigma phase formation in Cr- and V-containing high entropy alloys. *Mater. Res. Lett.* **1**, 207–212 (2013).
23. **D. Tabor**: The hardness and strength of metals. *J. Inst. Met.* **79**, 1–18 (1951).
24. **R.S. Ganji, P.S. Karthik, K.B.S. Rao, and K.V. Rajulapati**: Strengthening mechanisms in equiatomic ultrafine grained AlCoCrCuFeNi high-entropy alloy studied by micro- and nanoindentation methods. *Acta Mater.* **125**, 58–68 (2017).
25. **R. Sriharitha, B.S. Murty, and R.S. Kottada**: Alloying, thermal stability and strengthening in spark plasma sintered Al$_x$CoCrCuFeNi high entropy alloys. *J. Alloys Compd.* **583**, 419–426 (2014).
26. **G.K. Williamson and R.E. Smallman**: Dislocation densities in some annealed and cold-worked metals from measurements on the X-ray debye-scherrer spectrum. *Philos. Mag.* **1**, 34–46 (1956).
27. **R. Labusch**: Statistical theories of solid solution hardening. *Acta Metall.* **20**, 917–927 (1972).
28. **O.N. Senkov, J.M. Scott, S.V. Senkova, F. Meisenkothen, D.B. Miracle, and C.F. Woodward**: Microstructure and elevated temperature properties of a refractory TaNbHfZrTi alloy. *J. Mater. Sci.* **47**, 4062–4074 (2012).